Applied Surface Science 650 (2024) 159140

Contents lists available at ScienceDirect

Applied Surface Science

journal homepage: www.elsevier.com/locate/apsusc

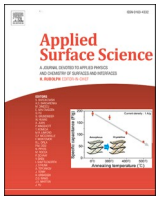

Full Length Article

Effects of high-temperature thermal reduction on thermal conductivity of reduced graphene oxide polymer composites

Yun Seon Lee [a,b,1], Nam Ryeol Kim [a,c,1], Sang Ki Park [a], Yong-il Ko [a], Yunjae Shin [d], Beomjoo Yang [d,*], Cheol-Min Yang [a,*]

[a] Institute of Advanced Composite Materials, Korea Institute of Science and Technology (KIST), 92 Chudong-ro, Wanju-gun, Jeollabuk-do 55324, Republic of Korea
[b] Department of Chemical Engineering, Inha University, 100 Inha-ro, Nam-gu, Incheon 22212, Republic of Korea
[c] Department of Polymer Engineering, Graduated School, Chonnam National University, 77 Yongbong-ro, Buk-gu, Gwangju 61186, Republic of Korea
[d] School of Civil Engineering, Chungbuk National University, 1 Chungdae-ro, Seowon-gu, Cheongju 28644, Republic of Korea

ARTICLE INFO

Keywords:
Reduced graphene oxide
Thermal reduction
Polymer composite
Thermal conductivity

ABSTRACT

The graphitic crystalline structure of reduced graphene oxide (rGO) can be improved by high-temperature thermal reduction at various heat-treatment temperatures ranging from 1000 to 2500 °C. The crystallinity significantly increased with increasing heat-treatment temperature. The electrical conductivities of the rGOs heat-treated at 2000 and 2500 °C (*h*-rGO-2000 and *h*-rGO-2500, respectively) were similar to those of commercial graphite. The isotropic thermal conductivity of rGO/epoxy composite with 10 wt% *h*-rGO-2500 (2.56 W/mK) was 11.6 times higher than that of pristine rGO (*p*-rGO; 0.22 W/mK) and significantly superior to those of epoxy composites with commercial graphite (0.82 W/mK) and mesophase pitch-based carbon fibers (MPCFs; 1.29 W/mK). Moreover, owing to the synergistic effect operating in the MPCF–*h*-rGO hybrid filler in epoxy composites, this combination of fillers increased the thermal conductivity to a greater extent than the MPCF–*p*-rGO hybrid filler. Optimum synergistic effects on the isotropic and in-plane thermal conductivities were achieved with an MPCF:*h*-rGO-2000 weight ratio of 49:1 (11.90 and 17.93 W/mK, 1.48 and 1.85 times higher than 8.02 and 9.69 W/mK for MPCF–*p*-rGO, respectively). Finally, a machine learning method that could predict and optimize the properties of rGOs based on their heat-treatment temperatures and material compositions was developed.

1. Introduction

Electronic devices have been downsized, integrated, and functionalized owing to rapid development in the electronics industry, with a consequent improvement in the performance of such devices. The recent popularization of electric vehicles and emergence of autonomous vehicles have significantly increased the demand for efficient heat dissipation technology that ensures the safety, reliability, and durability of electronic devices and next-generation vehicles by dissipating the heat generated during device operation [1–4]. Several studies have addressed this demand by developing high-performance heat dissipation materials [1–6]. Heat transfer materials with high thermal conductivities, such as metals and ceramics, are widely used to suppress the temperature rise of various components; however, these materials are heavy, expensive, and have poor formability and thus limited design freedom. Polymer composites have, therefore, been considered as alternative heat transfer materials for heat dissipation and thermal management applications [5] owing to their light weight, excellent formability, design freedom, low manufacturing costs, and high corrosion resistance [1,3,5,7–10].

Despite such numerous advantages, the intrinsic thermal conductivity of neat polymers (0.1–1.05 W/mK) are typically considerably lower than those of carbonaceous, metallic, and ceramic materials [1–3]. Hence, numerous studies have reported on investigating ways to increase the thermal conductivity of polymers [1–3]. Lightweight polymer-based heat dissipation materials are commonly prepared by combining polymer matrices with micro- and nanoscale carbonaceous fillers having high thermal conductivity, including mesophase pitch-based carbon fibers (MPCFs), graphite, expanded graphite (EG), graphene nanoplatelets (GNPs), reduced graphene oxide (rGO), and carbon nanotubes (CNTs) [7–12]. The thermal conductivity of such polymer

* Corresponding authors.
E-mail addresses: byang@chungbuk.ac.kr (B. Yang), cmyang1119@kist.re.kr (C.-M. Yang).
[1] These authors contributed equally to this work.

https://doi.org/10.1016/j.apsusc.2023.159140
Received 25 September 2023; Received in revised form 5 December 2023; Accepted 13 December 2023
Available online 19 December 2023

composites strongly depends on the properties of the fillers, particularly their shape, size, and intrinsic thermal conductivity, as well as their loading amount, dispersion state, and orientation degree in the polymer matrix [6–14]. The fabrication of carbon/polymer composites with excellent heat transfer capability requires a large loading of thermally conductive fillers, which can significantly deteriorate the mechanical properties and processability of the composites relative to those of the corresponding neat polymers. Therefore, optimization of the heat transfer pathways using the minimum loading of thermally conductive fillers in polymer matrices is crucial [15,16]. To this end, various studies have attempted to minimize the loading of such fillers in polymer composite systems while maintaining their heat transfer capabilities [17–19].

Among carbonaceous fillers, graphene, in particular, can greatly improve the thermal conductivity of polymer-based composites at low loadings owing to its high thermal conductivity and atomically thin two-dimensional structure [11,13,15–17]. Single-layered graphene exhibits an extremely high thermal conductivity of 5300 W/mK [20]. Therefore, graphene-based materials have attracted considerable attention from both academia and industries owing to their potential as thermally conductive fillers for more effective heat dissipation in polymer composites [11,21,22]. Molecular dynamics simulations conducted by Zhang et al. discovered that the thermal conductivity of defective graphene decreases as the number of defect sites increases [23]. Single- and few-layered graphene can be synthesized using several methods, including chemical and mechanical exfoliation, arc discharge, and chemical vapor deposition (CVD) [24–27]. However, the lack of a cost-effective means of mass producing high-quality graphene is a major impediment to expanding its applications. Conversely, rGO can be mass-produced by successively oxidizing and reducing graphite; however, while this method produces sheets with nanoscale stacking thicknesses and microscale lateral areas, it also introduces various defect sites and O-containing functional groups onto the rGO sheets, which unexpectedly and significantly reduces their thermal conductivity [28,29]. Despite considerable efforts to enhance the thermal conductivity of rGO/polymer composites by improving the quality of defective rGO and increasing the interfacial bonding force between rGO and the polymer matrix [28–31], the resulting conductivities are insufficient to meet the requirements of heat dissipation applications. Therefore, for cost-effective designing of thermally conductive polymer composites having optimal performance, it is necessary to determine a trade-off between the manufacturing costs (thermal reduction cost of rGO) and product quality (thermal conductivity of polymer composite).

In this study, rGO was heat-treated at various high temperatures (*h*-rGO) to alter its graphitic crystalline structure and improve its thermal conductivity. We then investigated changes in the structural and physical characteristics of the resulting rGOs after thermal reduction as a function of temperature, which was increased ranging from 1000 to 2500 °C in 500 °C increments. Epoxy-based composites loaded with pristine rGO (*p*-rGO) and *h*-rGOs as thermally conductive fillers were also fabricated, and their heat transfer properties were examined according to the thermal reduction temperature of the rGOs. The heat transfer performance of the *h*-rGO/epoxy composites was compared to that of composites loaded with commercial thermally conductive fillers. Furthermore, Gaussian process regression (GPR) method of machine learning (ML) was introduced to predict and optimize the material characteristics of rGOs and rGO/epoxy composites with various applied temperatures and composite compositions. We expect this study to provide significant beneficial information regarding the industrial manufacturing of thermally conductive polymer composites containing rGOs.

2. Experimental section

2.1. Preparation of thermally conductive epoxy-based composites

p-rGO (rGO-V30, Standard Graphene Inc., Korea), graphite flakes (~325 mesh, 99.8%, Alfa Aesar Co. Inc., USA), milled MPCFs (11-μm diameter, 200-μm length, Dialead, K223HM, Mitsubishi Plastic Inc., Japan), and multi-walled CNTs (MWCNTs; average diameter of 50–80 nm, average length of 10–20 μm, US4315, US Research Nanomaterials Inc., USA) were purchased from their respective suppliers. *p*-rGO mounted on a carbon crucible was heat-treated in a furnace from 25 °C to 1000, 1500, 2000, or 2500 °C for 1 h in an Ar atmosphere. The resulting powders were labeled *h*-rGO-1000, *h*-rGO-1500, *h*-rGO-2000, and *h*-rGO-2500, respectively. Samples were heated at 10 °C min^{-1} from 25 °C to 2000 °C, while the heating rate was reduced to 5 °C min^{-1} between 2000 and 2500 °C (Fig. S1).

The epoxy resin (bisphenol A diglycidyl ether, BADGE, YD-128) and curing agent (polyoxyalkylene diamine, D-230) were purchased from Kukdo Chemical Co. Ltd. (Korea). The weight ratio of the epoxy resin to the curing agent was 7:3. The epoxy resin was diluted with acetone before being mixed with the rGO fillers to ensure homogeneous dispersion of the fillers. The *p*-rGO and *h*-rGO fillers were then separately added to these mixtures at loadings of 1, 5, and 10 wt%. These loaded mixtures were mechanically stirred for 0.5 h followed by ultrasonication at a frequency of 40 kHz and a power of 300 W for 0.5 h. The as-obtained mixtures were dried on a hot plate at 80 °C for 2 h to remove any remaining acetone. The curing agent was then added, and the dried mixtures were again mechanically stirred for 0.5 h. Finally, the mixtures were cured at 100 °C for 3 h in a hot press equipped with a mold with a diameter of 18 mm and a thickness of 2 mm.

2.2. Characterization

The material properties of the *p*-rGO and *h*-rGOs were characterized using micro-Raman spectroscopy with an excitation wavelength of 514 nm (inVia Reflex Raman microscope, Renishaw, UK) and X-ray photoelectron spectroscopy (XPS, K-Alpha, Thermo Scientific, USA) with an Al K_α X-ray source under vacuum ($<10^{-8}$ Pa). X-ray diffraction (XRD) patterns were measured using an X-ray diffractometer (SmartLab, Rigaku, Japan) with conventional Cu K_α radiation at a wavelength of 0.154 nm and equipped with a Bragg diffraction setup. The electrical conductivities of the rGO powder samples were measured using a powder resistivity measurement system (HPRM-M2, Hantech, Korea). The morphologies of the rGOs and composites were characterized using field-emission scanning electron microscopy (FE-SEM, Nova NanoSEM 450, FEI, USA). For morphological analysis, the sample powders were placed on the carbon tape attached to the holder and subsequently blown using an air blower.

The thermal conductivities of the epoxy-based composites were measured using a thermal constants analyzer (TPS 2500S, Hot Disk AB, Sweden) in accordance with ISO 22007–2 and calculated using the Fourier equation [32]. The measurements were conducted using the isotropic module (for the average thermal conductivity of the specimens), anisotropic module (for direction-dependent thermal transport properties along and perpendicular to the main axis of uniaxial materials), and slab module (for the in-plane thermal conductivity of the specimens). This approach was employed to compare and examine the thermal conductivity behaviors of the epoxy-based composites. The volumetric heat capacity required for the anisotropic module was determined via differential scanning calorimetry (DSC, DSC 214 polyma, Netzsch, Germany) and an electronic balance utilizing the buoyancy method. Temperature variations on the surfaces of the molded and cured rGO/epoxy composite specimens during heating were observed using a surface temperature monitoring system (GR-STMS-1901, GyoRin Inc., Korea), equipped with an infrared thermal camera (FLIR T530, Wilsonville, USA). Thermal images of these composites were recorded

for 120 s. Dynamic mechanical analysis (DMA) was performed using a DMA Q800 (TA Instruments, USA) at a constant frequency of 1 Hz in film-tension mode over the range of 25–250 °C, with a heating rate of 3 °C min^{-1}. The DMA specimens with a rectangular shape (30.0 × 5.0 × 0.4 mm^3) were used.

3. Gaussian process machine learning

An ML simulation with diverse variables was performed based on the experimental results to predict the optimal rGO candidate. ML is a technique for building a model by learning the tendency between the input and output data. The GPR considered in this study was a non-parametric Bayesian regression method that used the properties of the Gaussian process, which can be defined as follows:

$$P(y \mid f, X) \sim N(y \mid H\beta + f, \sigma^2 \boldsymbol{I}) \tag{1}$$

with

$$X = \begin{pmatrix} x_1^T \\ x_2^T \\ \vdots \\ x_n^T \end{pmatrix}, \quad y = \begin{pmatrix} y_1 \\ y_2 \\ \vdots \\ y_n \end{pmatrix}, \quad H = \begin{pmatrix} h(x_1^T) \\ h(x_2^T) \\ \vdots \\ h(x_n^T) \end{pmatrix}, \quad f = \begin{pmatrix} f(x_1) \\ f(x_2) \\ \vdots \\ f(x_n) \end{pmatrix} \tag{2}$$

where X and y are the training sets, H is a set of basis functions, f denotes the joint distribution of the latent variables, β is a coefficient estimated from the experimental data, and σ^2 is the error variance. The GPR model is a non-parametric probabilistic model constructed using the function of the mean and covariance predicted from the uncertain distribution set. Predictions are made by calculating the probability of data having a similar distribution rather than by setting one point for predictions. Hence, the covariance function that expresses the distribution of the data is significant, and the performance of the model is determined by the assumption of the covariance function.

The GPR is a non-parametric probabilistic model that is based on the training set drawn from the disorganized distribution. In GPR, the definition of the mean and covariance functions, with regard to the disorganized dataset, was the most significant on the model performance. Herein, the uncertainty of the dataset was set to be a covariance, and four approaches were proposed for estimating the covariance: rational quadratic, Matern multiplying 5/2, squared exponential, and exponential. In addition, scale standardization of the dataset was also conducted to improve the model performance. In the preliminary test, the GPR with the exponential covariance function produced the most accurate results, and the same methodology was applied in all processes.

Predictive models based on conventional regression techniques can be easily distorted by the distribution of data or outliers. By contrast, GPR exists as a multivariate Gaussian through an overlapped distribution, and the reliability of the prediction can be further improved by interpolating the predicted value. In this study, the output values describe the electrical and thermal conductivities. The input variables for electrical conductivity were defined as the pressure (P) and heat-treatment (HT) temperature (T), while those for thermal conductivity were set as the contents of rGOs (ϕ_G) and MPCFs (ϕ_C) and the HT temperature (T). Fig. 1 shows a conceptual diagram of the corresponding GPR method employed in this study.

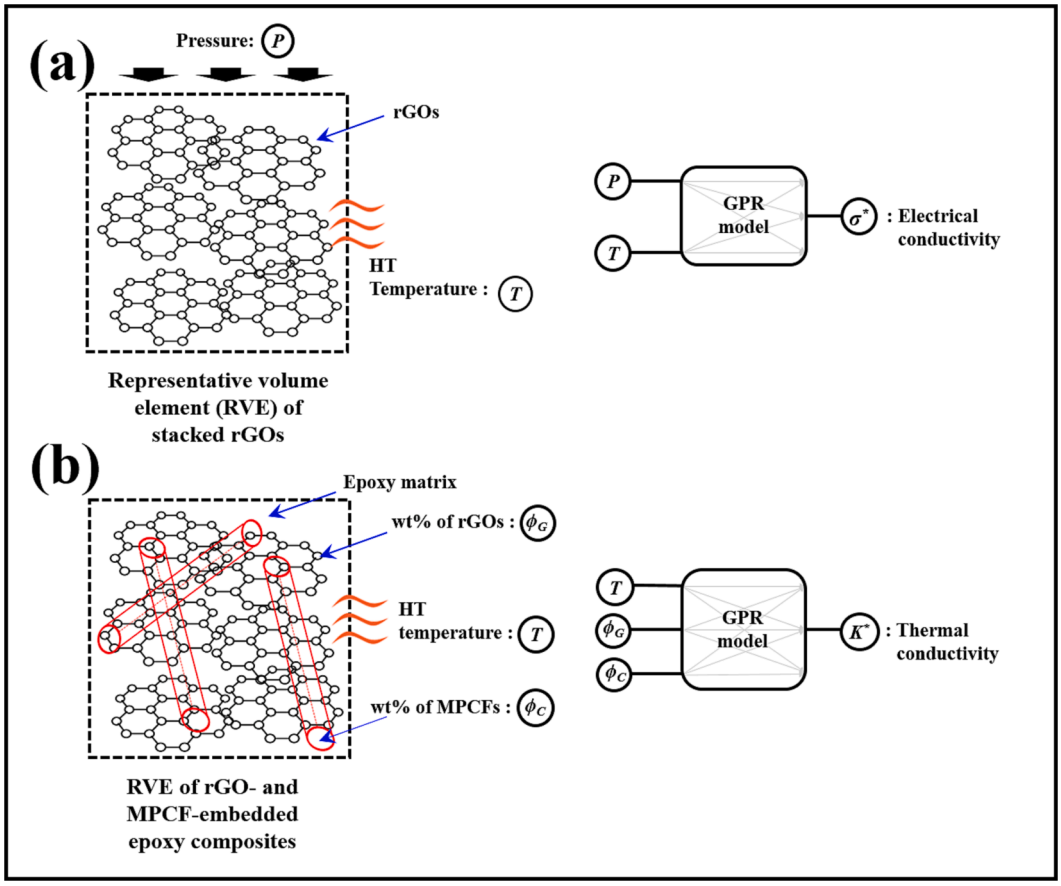

Fig. 1. Schematic illustrations of the GPR methods for (a) stacked rGOs and (b) rGO- and MPCF-embedded epoxy composites.

4. Results and discussion

4.1. Characterization of rGOs reduced at high temperature

The structural properties of *p*-rGO and *h*-rGOs were analyzed using Raman spectroscopy (Table S1 and Fig. 2a). The spectra of all samples showed two strong peaks corresponding to the *D*- and G-bands at approximately 1,360 cm^{-1} and 1,590 cm^{-1}, respectively. The *D*- and *G*-bands are associated with defect-induced disorder and graphitic sp^2 carbon structures, respectively, in carbonaceous materials. Thus, concentration of structural defects in rGO is indicated by the I_D/I_G ratio [28]. The *D*- and *G*-bands of *p*-rGO showed similar intensities (I_D/I_G ratio of 0.93), while the I_D/I_G ratio of *h*-rGO-1000 was higher at 1.34, which may be explained by the release of CO gas owing to the thermal decomposition of C–O–C bonds. Consequently, the hexagonal structure of the adjacent C=C bonds was broken, thereby increasing the number of defects in the rGO structure [29,33]. Conversely, at an HT temperature of 1500 °C and higher, the I_D/I_G ratio decreased proportionally with the HT temperature, and the peaks corresponding to the *D*- and *G*-bands became sharper. This indicates that the O-containing functional groups of *p*-rGO were removed at 1500 °C and above, thereby reducing the defect concentration of *p*-rGO [34]. The I_D/I_G ratio of *h*-rGO-2500 (0.03) was slightly lower than that of *h*-rGO-2000 (0.09), indicating that most of the O-containing functional groups were removed by HT at 2000 °C, and the defects were partially restored. In addition, the spectra of *h*-rGO-2000, *h*-rGO-2500, and commercial graphite exhibited a weak *D'*-band at approximately 1620 cm^{-1}. Although this band appears to be a shoulder of the *G*-band, it originates from the disordered structures of graphitic materials [35]. Therefore, the *D'*-band contributed to the peak shift of the *G*-band in this study.

The *G*-band of *h*-rGO-1000 blue-shifted with respect to that of *p*-rGO, from 1588 cm^{-1} to 1592 cm^{-1}. In addition, the intensity of the *D'*-band, which may have partially merged with the G-band, increased owing to the increased number of defects in the rGO. Consequently, the *G*-band broadened and shifted to higher frequencies [36]. However, when *p*-rGO was heat-treated between 1500 and 2500 °C, the positions of the *G*-bands of *h*-rGO-1500, *h*-rGO-2000, and *h*-rGO-2500 red-shifted to 1587, 1582, and 1581 cm^{-1}, respectively, from that of *p*-rGO (1588 cm^{-1}), indicating that the *D'*-bands separated from the *G*-band as the HT temperature increased. Furthermore, the intensities of the *D'*-bands decreased significantly with increasing HT temperature owing to the restoration of the hexagonal structure of *p*-rGO and consequent reduction in the number of defects. Moreover, the reduction in the width of the *G*-band peak, red shift in its position, and reduction in the I_D/I_G ratio all strongly indicate a higher level of graphitization [35]. The structural parameters determined from the Raman spectra clearly revealed that the structure of the *h*-rGOs became increasingly similar to that of commercial graphite with increasing HT temperature.

The spectra of *p*-rGO and *h*-rGO-1000 showed weak *2D*-bands and (*D* + *G*)-bands at approximately 2700 cm^{-1} and 2950 cm^{-1}, respectively (Table S1 and Fig. 2a). Further, *h*-rGO-1500 showed broad *2D*-band and (*D* + *G*)-band peaks, whereas *h*-rGO-2000 and *h*-rGO-2500 showed more distinct *2D*-band peaks, in addition to the (*D* + *G*)-band peak. The *2D*-band is attributed to double resonance transitions, which produce two phonons with opposite momenta, while the shape and position of the band depend on the number of graphene layers. In addition, the (*D* + *G*) combined band is influenced by the defect-induced disorder in the graphitic materials, indicating the high level of graphitization in *h*-rGO-2000 and *h*-rGO-2500 [37]. The *G*-band and *2D*-band are associated with sp^2-hybridized C=C bonds in the graphitic structure. The broad *2D*-bands of *p*-rGO and *h*-rGO-1000 exhibited extremely low intensities, and became increasingly sharp as the HT temperature increased. The I_{2D}/I_G ratio is related to the degree to which the hexagonal graphitic structure is restored [38]. *p*-rGO exhibited an I_{2D}/I_G ratio of 0.16 owing to the extremely weak, broad *2D*-band, which indicates that the regular crystal symmetry of the hexagonal structure is destroyed by a number of defects that interfere with the resonance conditions [39]. Notably, the I_{2D}/I_G ratio of *p*-rGO increased from 0.16 to 0.21, 0.54, 0.95, and 0.91 at HT temperatures of 1000, 1500, 2000, and 2500 °C, respectively, indicating that the hexagonal structure was restored by the removal of defects and O-containing functional groups, while a few layers of the rGO sheets were restacked [40]. As a result, the interlayer interaction between the rGO sheets increased owing to the improved crystallinity of their graphitic structure, thereby increasing the intensity of the *2D*-band (Fig. 2a).

The shape and intensity of the *2D*-bands in the spectra of the *h*-rGOs differed slightly from those of the 2*D*-band in the spectrum of commercial graphite. The *2D*-bands of *h*-rGO-2000, *h*-rGO-2500, and commercial graphite were located at 2706, 2708, and 2713 cm^{-1}, respectively, and their respective I_{2D}/I_G ratios were 0.95, 0.91, and 0.53. The *2D*-band in the spectrum of graphite typically consists of two components, $2D_1$ and $2D_2$, whereas that in single-layered graphene consists of only one strong $2D_1$ component [41]. The deconvoluted *2D*-bands of *h*-rGO-2000 and *h*-rGO-2500 showed features typical of few-layered graphene with a larger $2D_1$-band, whereas that of commercial graphite showed a larger $2D_2$-band, typical of graphite (Fig. S2). Therefore, although the rGO sheets were restacked and graphitized by high-temperature thermal reduction, few-layered graphene structures formed rather than the graphite structure.

The crystallization of the rGO powders was confirmed using XRD spectroscopy. The XRD patterns of all samples (Fig. 2b) showed peaks at approximately 26° corresponding to the (0 0 2) plane, which was

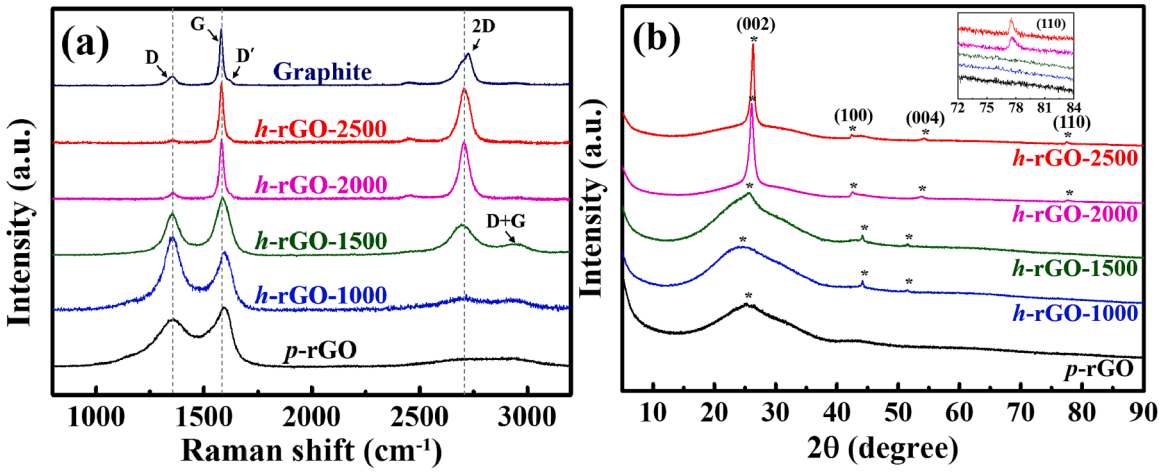

Fig. 2. (a) Raman spectra of *p*-rGO, *h*-rGOs, and commercial graphite and (b) XRD patterns of *p*-rGO and *h*-rGOs. Inset: enlarged (1 1 0) peaks.

attributed to the graphene-like structure. The interlayer spacing (d_{002}) of the rGO powders can be calculated from the shift in the (0 0 2) peak position by Bragg's law ($d_{002} = \lambda/(2\sin\theta)$) using the X-ray wavelength (λ =0.154 nm for Cu K_α X-ray radiation) and scattering angle (θ) [35]. The 2θ position of the (0 0 2) peak shifted from 25.22° to 26.33° as the HT temperature was increased to 2500 °C (Fig. 2b and Table 1), indicating that the d_{002} decreased from 0.353 to 0.338 nm. The XRD patterns of all samples except *p*-rGO exhibited weak peaks at approximately 42° and 54° corresponding to the (1 0 0) and (0 0 4) planes, respectively. In addition, the spectra of *h*-rGO-2000 and *h*-rGO-2500 showed extremely weak peaks at approximately 78°, assigned to the (1 1 0) plane. These results suggest that the crystalline lattice structure is formed by the removal of O-containing functional groups from the surface of *p*-rGO during high-temperature thermal reduction. In addition, the crystallinity of *p*-rGO, *h*-rGO-1000, and *h*-rGO-1500 was confirmed by the full width at half maximum (FWHM) values of their (0 0 2) peaks (12.961, 12.430, and 11.154, respectively). These extremely high FWHM values are associated with residual O-containing functional groups and defects in the rGO samples, resulting in an amorphous carbon structure. In contrast, the FWHM values of *h*-rGO-2000 and *h*-rGO-2500 significantly decreased to 0.781 and 0.561, respectively, indicating that a more crystalline graphitic structure is formed by the reduction of *p*-rGO at 2000 and 2500 °C [36].

FE-SEM images of *p*-rGO, *h*-rGOs, and commercial graphite (Fig. S3) reveal that the morphologies of *p*-rGO and *h*-rGOs are typical of a single layer or a few layers of crumpled graphene sheets (Fig. S3a–e). The degree of clumping of the graphene sheets was noticeably less extensive in *h*-rGO-2000 and *h*-rGO-2500. In addition, *h*-rGO-2000 and *h*-rGO-2500 exhibited loosely stacked layer structures with a smaller interlayer spacing. The FE-SEM image of the commercial graphite powder (Fig. S3f) clearly showed the typical morphology of graphite, with smooth, flat graphene sheets densely stacked together with microscale thickness, in contrast to the morphologies of *p*-rGO and *h*-rGOs.

The surface chemical compositions of *p*-rGO and *h*-rGOs were confirmed using XPS (Fig. 3). The wide-scan XPS spectra of *p*-rGO and *h*-rGOs indicate the presence of C and O (Fig. 3a) and provide further evidence of the restoration of the crystalline structure, in good agreement with the Raman and XRD results. The O 1 s peaks (at approximately 533 eV) of the *h*-rGOs were significantly weaker than those of *p*-rGO. The surface O content of *p*-rGO was estimated as 13.45 at%, which significantly decreased as the HT temperature increased, reaching a minimum of 0.91 at% at 2500 °C (Table 1), indicating the successful removal of the O-containing functional groups. This reduction in O content resulted in a significant reduction in the O/C ratio of *h*-rGO-2500 (0.009) relative to that of *p*-rGO (0.155). This result was confirmed by the C 1 s spectra. The deconvoluted C 1 s spectrum of *p*-rGO showed five peaks at approximately 284.5, 284.9, 286.3, 287.0, and 290.1 eV, which were assigned to the sp^2-hybridized carbon (C=C), sp^3-hybridized carbon (C–C), epoxide (C–O–C), carbonyl (C=O), and carboxyl (HO–C=O) functional groups, respectively (Fig. 3b) [42]. A comparison of the relative sp^2/sp^3 C peak intensity ratios confirmed the change in the carbon bonding states of the rGOs after HT. As the HT temperature increased to 2500 °C, the sp^2/sp^3 C ratio significantly increased from 1.08 to 13.58, indicating the formation of an increasingly graphitic structure. After HT, most of the O-containing functional groups were successfully removed (Fig. 3b–f). In particular, the number of C–O bonds in *h*-rGO-1000 was significantly lower, indicating a higher number of defects in its graphene layers. This observation is consistent with the results of Raman spectroscopy. In addition, the ($\pi \rightarrow \pi^*$) shakeup satellite peak at approximately 291 eV appeared in the spectra of both *h*-rGO-2000 and *h*-rGO-2500 (Fig. 3e, f), indicating that the delocalized π conjugation was restored in the *h*-rGOs [43].

The electrical conductivities of the powder samples of *p*-rGO, *h*-rGOs, and commercial graphite were measured across a range of pressures (Fig. S4). The electrical conductivities of each powder sample increased as the applied pressure was increased owing to the reduced contact area between adjacent particles. The electrical conductivity of the *p*-rGO powder was typically considerably lower than that of the commercial graphite, used as a precursor in rGO synthesis, owing to the increased number of defects introduced during the synthesis procedure and the increased interfacial area at the interparticle junctions of rGO. However, the electrical conductivities of the *h*-rGO powders increased proportionally with the HT temperature, increasingly approaching that of commercial graphite. These results are associated with the removal of O-containing functional groups and the restoration of defects in the hexagonal structure of rGO after high-temperature thermal reduction, as corroborated by the Raman, XRD, and XPS results.

4.2. *Effects of high-temperature thermal reduction of GO on the thermal conductivity of epoxy-based composites*

Fig. 4a presents the isotropic thermal conductivities of neat epoxy and rGO/epoxy composites containing *p*-rGO and *h*-rGOs as functions of the HT temperature and filler content. The *p*-rGO fillers did not significantly improve the thermal conductivity of the *p*-rGO/epoxy composites, regardless of the loading. The marginal improvement in thermal conductivity observed for *p*-rGO/epoxy composites upon the addition of *p*-rGO fillers can be ascribed to several factors. First, the incomplete reduction of *p*-rGO resulted in the preservation of numerous defects within the rGO sheets even after the reduction process. Further, the weak interlayer interaction between *p*-rGO sheets might render the plate-like *p*-rGO morphology susceptible to deformation during composite fabrication, leading to a decrease in its specific surface area. Consequently, the formation of an effective filler–filler network might be hindered, even at a filler content of 10 wt%, and the thermal conductivity characteristics of *p*-rGO resembled that of neat epoxy (0.23 W/mK) within the experimental error range. It is expected that beyond a filler content of 10 wt%, a percolation threshold network will effectively form, enhancing interparticle connectivity and the thermal conductivity properties of the composite material. The thermal conductivity of the rGO/epoxy composite loaded with 10 wt% *h*-rGO-1000 increased by only ~ 44% with respect to that of neat epoxy (from 0.23 to 0.33 W/mK). In contrast, the thermal conductivities of composites loaded with *h*-rGO-1500, *h*-rGO-2000, and *h*-rGO-2500 increased as the filler content increased to 10 wt%. In particular, the magnitudes of the increase in thermal conductivity of rGOs heat-treated at 1500 °C and above were

Table 1
(0 0 2) peak positions, FWHMs, and d_{002} values obtained from the XRD patterns of *p*-rGO and *h*-rGOs. Atomic compositions of *p*-rGO and *h*-rGOs determined from XPS spectra.

	XRD pattern			XPS spectra			
	2θ (0 0 2)	FWHM	d_{002} (nm)	C (at%)	O (at%)	O/C	sp^2/sp^3 C ratio
p-rGO	25.22	12.961	0.353	86.55	13.45	0.155	1.08
h-rGO-1000	25.26	12.430	0.352	93.68	6.32	0.068	6.31
h-rGO-1500	25.47	11.154	0.349	95.37	4.63	0.049	7.37
h-rGO-2000	26.06	0.781	0.342	99.04	0.96	0.010	10.44
h-rGO-2500	26.33	0.561	0.338	99.09	0.91	0.009	13.58

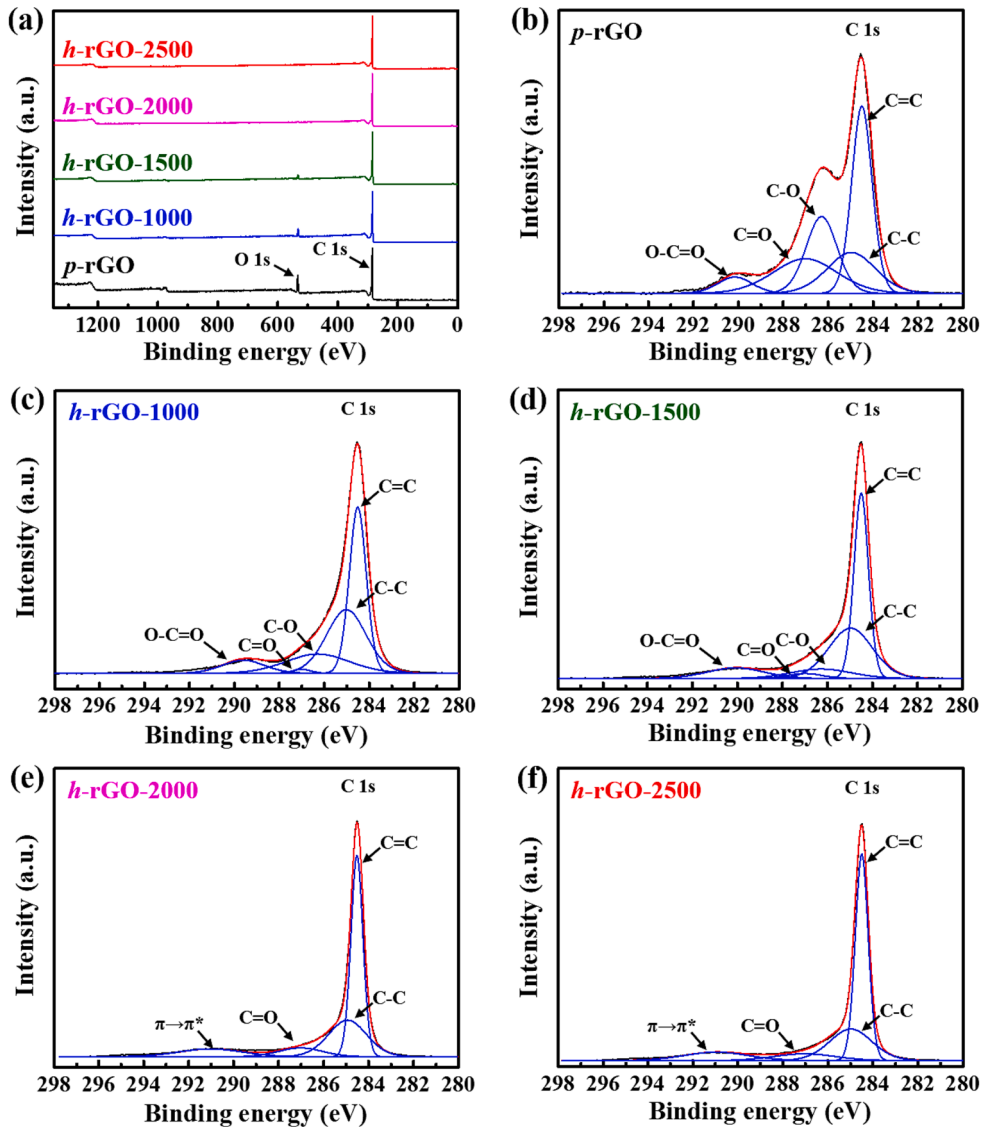

Fig. 3. (a) XPS survey spectra and (b–f) high-resolution C 1s spectra of *p*-rGO and *h*-rGOs.

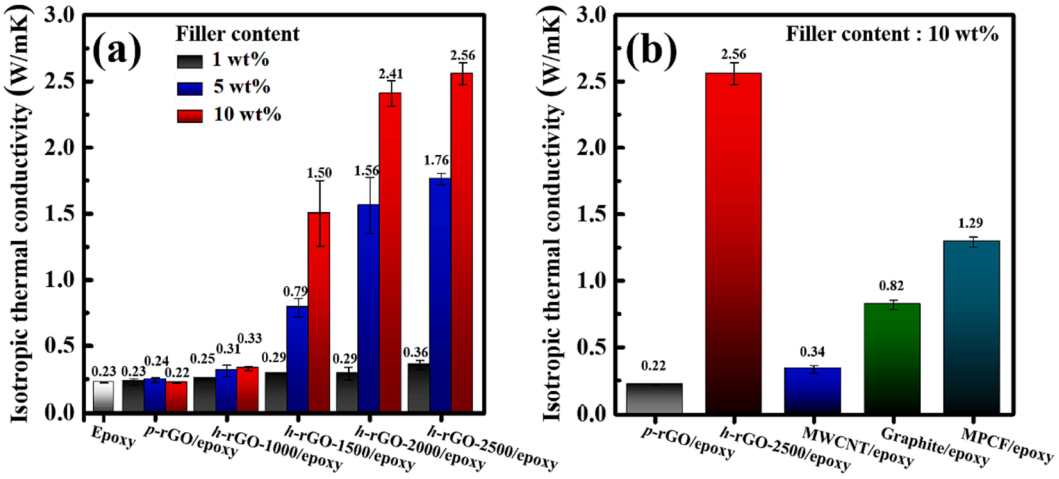

Fig. 4. Isotropic thermal conductivities of neat epoxy resin and epoxy-based composites reinforced with (a) *p*-rGO and *h*-rGOs of different contents and (b) MWCNTs, graphite, and MPCFs.

significantly larger than those of the rGO heat-treated at 1000 °C. The thermal conductivities of the rGO/epoxy composites with *p*-rGO increased significantly with increasing HT temperature. With an rGO filler content of 1 wt%, the thermal conductivities of the composites gradually increased from 0.23 to 0.36 W/mK (57% increase) with increasing HT temperature. Conversely, with *h*-rGO-2500, the thermal conductivities of the rGO/epoxy composites with filler contents of 5 and 10 wt% increased from 0.24 to 1.76 W/mK and from 0.22 to 2.56 W/mK, respectively, representing a 7.3-fold and 11.6-fold increase, respectively. In particular, the thermal conductivity of the *h*-rGO-2500/epoxy composite with 10 wt% rGO was approximately 11.6 times higher than that of the composite with 10 wt% *p*-rGO. Various defects, including heteroatoms, pentagonal or heptagonal carbon rings, and holes in the graphene structure of the rGO fillers are known to increase phonon scattering, thereby reducing their thermal conductivity [44]. As mentioned in section 4.1, high-temperature HT of *p*-rGO removed O-containing functional groups from the rGO surface and removed the defects in the hexagonal graphitic structure, thus increasing its thermal conductivity. Therefore, this significant increase in the thermal conductivity of the *h*-rGO-2500/epoxy composite is closely associated with the removal of defects in the rGOs during high-temperature thermal reduction, as supported by the Raman, XRD, and XPS analyses.

The isotropic thermal conductivity of the *h*-rGO-2500/epoxy composite was compared to those of epoxy-based composites containing commercial thermally conductive carbon fillers (Fig. 4b). The thermal conductivity of *h*-rGO-2500/epoxy composite containing 10 wt% *h*-rGO-2500 (2.56 W/mK) was approximately 753%, 212%, and 99% higher than those of epoxy-based composites containing MWCNTs (0.34 W/mK), graphite (0.82 W/mK), and MPCFs (1.29 W/mK), respectively. Even at a low *h*-rGO-2500 filler content of 5 wt% (Fig. 4a), the *h*-rGO-2500/epoxy composite exhibited higher thermal conductivity (1.76 W/mK) than the composites loaded with 10 wt% of the other carbon fillers. The extremely high thermal conductivity of the *h*-rGO-2500/epoxy composite can be attributed to the highly crystalline, thin, sheet-like graphitic structures with low apparent density observed in the *h*-rGOs. A comparison of the thermal conductivities of the *h*-rGO-2500/epoxy composite and the composites filled with commercial carbon fillers shows that the former clearly exhibits superior heat transfer performance. Moreover, the thermal conductivities of the epoxy composites containing 10 wt% of *h*-rGO-2000 and *h*-rGO-2500 were compared with those of existing polymer composites with graphene-based carbon fillers (EG, GNP, GO, and rGO) in Table 2 [45–53]. Especially, we calculated the thermal conductivity enhancement (TCE) efficiency of the epoxy composites to compare our results with those reported in previous studies. The TCE efficiency (η) of the epoxy composites can be calculated using the following equation [54]:

$$\eta\,(\%) = \frac{K - K_m}{\varphi_f K_m} \times 100\% \tag{3}$$

where K and K_m are the thermal conductivities of the composite and neat epoxy matrix, respectively, and φ_f denotes the filler mass fraction in the composite. The in-plane thermal conductivities of these composites increased to 4.30 W/mK (for *h*-rGO-2000) and 4.98 W/mK (for *h*-rGO-2500), with corresponding TCE efficiencies of 177.0% and 206.5%, respectively. Moreover, the through-plane thermal conductivities of the rGO/epoxy composites increased from 0.22 W/mK (neat epoxy) to 1.33 W/mK (for *h*-rGO-2000) and 1.71 W/mK (for *h*-rGO-2500), with corresponding TCE efficiencies of 50.5% and 67.7%, respectively. This finding suggests that the addition of *h*-rGOs improved the in-plane and through-plane thermal conductivities of the rGO/epoxy composites, with the improvement in the in-plane thermal conductivities being substantially higher. The TCE efficiencies of the *h*-rGO/epoxy composites synthesized in this study are greatly superior to those of the existing composites.

To evaluate the heat transfer capabilities of epoxy-based composites reinforced with 10 wt% *p*-rGO and *h*-rGOs, infrared thermal images and surface temperature variations of composite specimens laid on an isothermal hot plate at 100 °C were observed for 120 s using an infrared thermal camera (Fig. 5). All infrared thermal images of the composite surfaces showed a gradual increase in the surface temperature of the composite specimens, as indicated by the color change from blue to red. During heating, the images of the *h*-rGO/epoxy composite specimens turned red more rapidly than those of the *p*-rGO/epoxy composite specimens, and the rate at which the color changed increased with increasing HT temperatures. In addition, the surface temperatures of all the composite specimens increased with increasing HT temperature over the same heating duration. After heating the isothermal hot plate for 120 s, the *h*-rGO-2500/epoxy composite reached the highest surface temperature, demonstrating its superior heat transfer capability

Table 2
Thermal conductivities of epoxy-based composites reinforced with 10 wt% *h*-rGO-2000 and *h*-rGO-2500. The thermal conductivities of existing polymer composites with graphene-based carbon fillers are provided for comparison.

Filler type	Thermal conductivity (W/mK)	Loading (wt%)	TCE efficiency (%)	Matrix	Measurement method	Reference
rGO (*h*-rGO-2500)	2.56 (isotropic)	10	101.3	Epoxy	Hot disk	This work
	4.98 (in-plane)		206.5			
	1.71 (through-plane)		67.7			
rGO (*h*-rGO-2000)	2.41 (isotropic)	10	94.8	Epoxy	Hot disk	
	4.30 (in-plane)		177.0			
	1.33 (through-plane)		50.5			
EG	1.20	10	17.3	HDPE[a]	Hot disk	[45]
GNP	0.75	10	22.6	PVDF[b]	Hot disk	[46]
GNP	0.85 (cross-plane)	5	65.0	Epoxy	Laser flash	[47]
GNP	1.61	4	113.8	PEG[c]	Hot disk	[48]
GNP	2.21	10	86.1	Bio-based epoxy	Hot wire	[49]
GNP	0.36	4	11.8	PDMS[d]	Hot disk	[50]
GNP	0.50 (bulk)	10	23.3	CBT[e]	Hot disk	[51]
	1.20 (in-plane)		70.0			
GO[f]	0.29	10	3.2	PVDF	Hot disk	[52]
rGO	0.60	10	156.0	Epoxy	Hot disk	[53]

[a] HDPE: high-density polyethylene.
[b] PVDF: polyvinylidene fluoride.
[c] PEG: polyethylene glycol.
[d] PDMS: polydimethylsiloxane.
[e] CBT: cyclic butylene terephthalate.
[f] GO: graphene oxide.

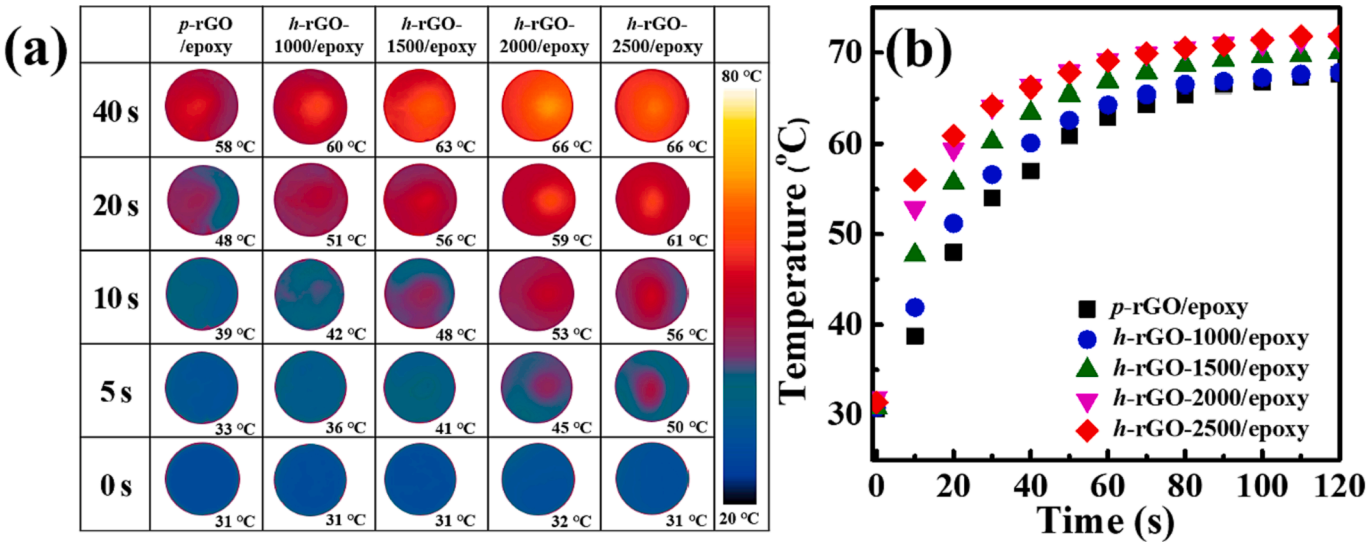

Fig. 5. Transient temperature responses during heating: (a) infrared camera images and (b) temperature–time profiles of the epoxy-based composites reinforced with 10 wt% *p*-rGO and *h*-rGOs.

compared to the other composites. The trend in the heat transfer capabilities of the rGO/epoxy composites was consistent with that in their thermal conductivities. These results clearly showed that the heat dissipation ability of the *h*-rGO/epoxy composites was far superior to that of the *p*-rGO/epoxy composite.

The mechanical properties of polymer-based composites vary with temperature, time, and frequency due to their viscoelasticity. Therefore, several researchers have reported on the mechanical properties of polymer-based composites using the DMA method, which is an effective tool to assess the storage modulus (E'), loss modulus (E''), and damping factor (tan δ, E''/E'), i.e., viscoelastic properties under stress and temperature [55,56]. The mechanical properties of the *h*-rGO/epoxy composites measured using DMA are shown in Fig. 6. The E' value refers to the stored elastic energy in the samples during deformation. The DMA curves showed E' values of neat epoxy and *h*-rGO/epoxy composites with varying *h*-rGO-2500 contents as a function of temperature, which showed a decreasing tendency over the entire temperature range due to softening of the polymer chains upon transition from a glassy to a rubbery state (Fig. 6a). The E' values of the *h*-rGO/epoxy composites at 25 °C increased from 1789.3 MPa for the neat epoxy to 2341.2, 3337.7, and 3449.0 MPa for the *h*-rGO-2500/epoxy composites loaded with 1, 5, and 10 wt% *h*-rGO-2500 contents, respectively. This is because the *h*-rGOs, having a wrinkled structure and large specific surface area, promote mechanical interlocking with the polymeric matrix, thereby restricting the mobility of the epoxy chains. However, the E' value of the 10 wt% *h*-rGO-2500/epoxy composite decreased sharply compared to the 5 wt% *h*-rGO-2500/epoxy composite, in accordance with the increasing temperature, due to the free volume increase of the epoxy matrix upon agglomeration of the fillers [55,57]. Tan δ is a measure of the energy dissipation of the samples, and its peak temperature is typically used to determine the glass transition temperature (T_g) of the samples. The peak temperatures of tan δ for the *h*-rGO/epoxy composites shifted to lower temperatures with increasing *h*-rGO-2500 content (Fig. 6b). The T_g values were decreased from 75.6 °C for the neat epoxy to 75.2, 72.3, and 65.2 °C for the *h*-rGO-2500/epoxy composites loaded with 1, 5, and 10 wt% *h*-rGO-2500 contents, respectively. The decrement in the T_g value with increasing *h*-rGO-2500 content was due to an increase in free volume between the filler and epoxy [58].

We previously demonstrated the pronounced synergistic effects in hybrid carbonaceous fillers containing MPCFs and rGO in enhancing the heat dissipation capability of polymer composites [59]. MPCFs with highly crystalline graphitic structures are used as thermally conductive reinforcements in heat dissipation composites owing to their extremely high thermal conductivity of approximately 1000 W/mK [59,60].

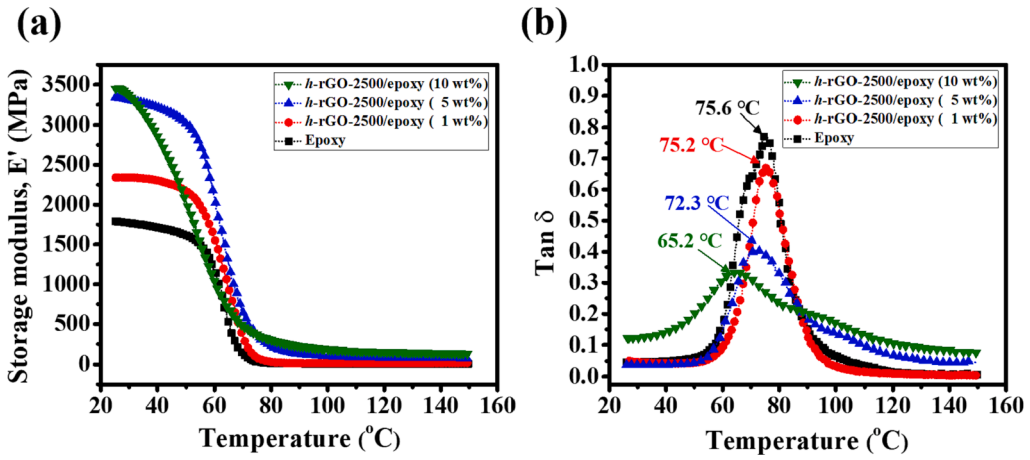

Fig. 6. (a) Storage modulus (E') and (b) tan δ plots of neat epoxy and *h*-rGO-2500/epoxy composites loaded with 1, 5, and 10 wt% *h*-rGO-2500 contents as a function of temperature.

Herein, the *h*-rGO-2000/epoxy composite was selected to evaluate the synergistic effects of the epoxy-based composites, loaded with hybrid fillers of MPCFs and *h*-rGOs, on the thermal conductivity enhancement from an economic point of view, as additional thermal reduction time (1.5 times) and energy consumption were required for the reduction of the *h*-rGO-2500 compared to the *h*-rGO-2000 (Fig. S1). In addition, the relative difference of thermal conductivity between the composites (*h*-rGO-2000/epoxy, *h*-rGO-2500/epoxy) was insignificant (Fig. 4a). Fig. 7 presents the isotropic and in-plane thermal conductivities of the epoxy-based composites containing various hybrid fillers with different weight ratios. The maximum synergistic effect on the isotropic and in-plane thermal conductivities of MPCF–rGO/epoxy composites was obtained at an MPCF:rGO weight ratio of 49:1. The isotropic and in-plane thermal conductivities of epoxy-based composites loaded with only MPCFs (50 wt%) were 5.32 and 7.33 W/mK, respectively, while those of the composites loaded with a hybrid of MPCFs (49 wt%) and *p*-rGO (1 wt%), were 8.02 and 9.69 W/mK (increases of approximately 51% and 32%, respectively), indicating the formation of effective heat transfer pathways by the thermal bridging effect of *p*-rGO nanosheets between neighboring MPCFs. Fig. S5 shows the cross-sectional FE-SEM images of the MPCF/epoxy and MPCF–rGO/epoxy composites, explaining the thermal bridging effect in further detail. For the MPCF/epoxy composite containing 50 wt% MPCFs, the epoxy matrix having low thermal conductive properties covered between the MPCFs, thereby disrupting thermal dissipation (Fig. S5a). However, when *h*-rGO-2000 (1 wt%) was added to the MPCF/epoxy composite, the mixture of the epoxy matrix and *h*-rGO-2000 fillers covered between the MPCFs, acting as a 'thermal bridge' (Fig. S5b). Therefore, it was confirmed that the addition of even 1 wt% *h*-rGO-2000 significantly improved the thermal conductivity of the MPCF–rGO/epoxy composite. However, the thermal conductivity of the MPCF–*p*-rGO/epoxy composites with rGO contents of 2 and 3 wt% decreased with increasing *p*-rGO content, indicating a reduced synergistic effect on the thermal conductivity owing to the agglomeration of rGO particles, which is in good agreement with our previous study [59]. The isotropic and in-plane thermal conductivities of the hybrid epoxy-based composites loaded with MPCFs (47–49 wt%) and *h*-rGO-2000 (1–3 wt%) exhibited similar trends to those observed in the composites loaded with MPCFs and *p*-rGO. However, the synergistic effect on the thermal conductivity enhancement significantly increased with respect to that of the MPCF–*p*-rGO/epoxy composites. The maximum synergistic effects on the isotropic and in-plane thermal conductivities were observed in epoxy composites with an MPCF:*h*-rGO-2000 weight ratio of 49:1 (11.90 and 17.93 W/mK, increases of approximately 124% and 145%, respectively).

Fig. 8 shows the cross-sectional FE-SEM images of the MPCF/epoxy composite with only MPCFs (50 wt%) and MPCF–rGO/epoxy composites with different MPCFs (47–49 wt%) and *h*-rGO-2000 contents (1–3 wt%) to discuss the maximum synergistic effect in further detail. The MPCF–rGO/epoxy composite, with an MPCF:*h*-rGO-2000 weight ratio of 49:1, exhibited the optimal synergistic effect because the *h*-rGO-2000 nanoparticles completely covered the MPCFs and formed thermal bridges (Fig. 8b). However, for the MPCF–rGO/epoxy composites containing more than 2 wt% *h*-rGO-2000, the synergistic effect was rather decreased, resulting in relatively low thermal conductivity. This was because when more than 2 wt% *h*-rGO-2000 (which is relatively bulky compared to the epoxy matrix) was loaded, the agglomeration of the *h*-rGO-2000 nanoparticles was promoted and the volume fraction occupied by the epoxy resin decreased. For this reason, it is difficult for *h*-rGO-2000 nanoparticles to completely cover the MPCFs (Fig. 8c, d). Consequently, unexpected voids (red circles in Fig. 8c, d) were formed around the MPCFs and the thermal bridges were insufficiently formed, resulting in a decreased synergistic effect.

4.3. Theoretical analysis of the thermal conductivity behavior in epoxy-based composites

Fig. 9 shows the electrical conductivity of the epoxy-based composites calculated using the ML-based GPR model. The pressure (*P*) and HT temperature (*T*) variables were set according to the observed experimental data and used as training values, and the corresponding results are shown in Fig. 9a. The model had a high degree of regularity in the present experiment, resulting in an extremely high correlation. Eq. (4) was derived to predict the electrical conductivity of the composites according to the two input values (*P* and *T*) of the GPR method:

$$\sigma^{*} = 9.3\cdot10^{-5}\left[(T+2P)^{2}+T^{2}P+P^{2}(P+4)\right]+3.5\cdot10^{-13}\cdot T^{2}P^{4}(T+2P) \\ -4\cdot10^{-10}\cdot T\cdot P^{2}\left[\cos(T)+0.8\right](T+2P)(T+8P) \quad (4)$$

where σ^{*} denotes the effective electrical conductivity of the composites, and *T* and *P* are the applied temperature and pressure during the rGO reduction process, respectively. Eq. (4) was then used to predict the electrical conductivity of the composites under conditions (T = 25, 1000, 1500, 2000, and 2500 °C; $P > 50$ MPa) that were not previously examined experimentally, as shown in (Fig. 9b). The model predicted that a higher electrical conductivity would be achieved at higher HT temperatures; however, the efficiency decreased with increasing temperature. The electrical conductivity tended to increase gradually as the applied pressure increased, whereas the slope decreased slightly.

The GPR-based thermal conductivity predictions are similar to the electrical conductivity predictions (Fig. 10). Using the experimental results as training data, the following Eqs. (5) and (6) were derived to

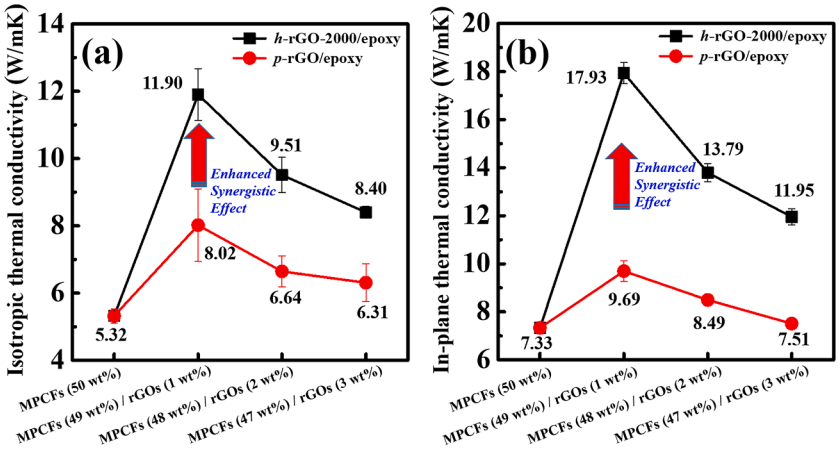

Fig. 7. (a) Isotropic and (b) in-plane thermal conductivities of epoxy-based composites containing MPCF–rGO hybrid fillers of MPCFs (200 μm) and different contents (0 to 3 wt%) of *p*-rGO and *h*-rGO-2000. The total loadings of MPCFs and rGOs in the epoxy-based composites were adjusted to 50 wt%.

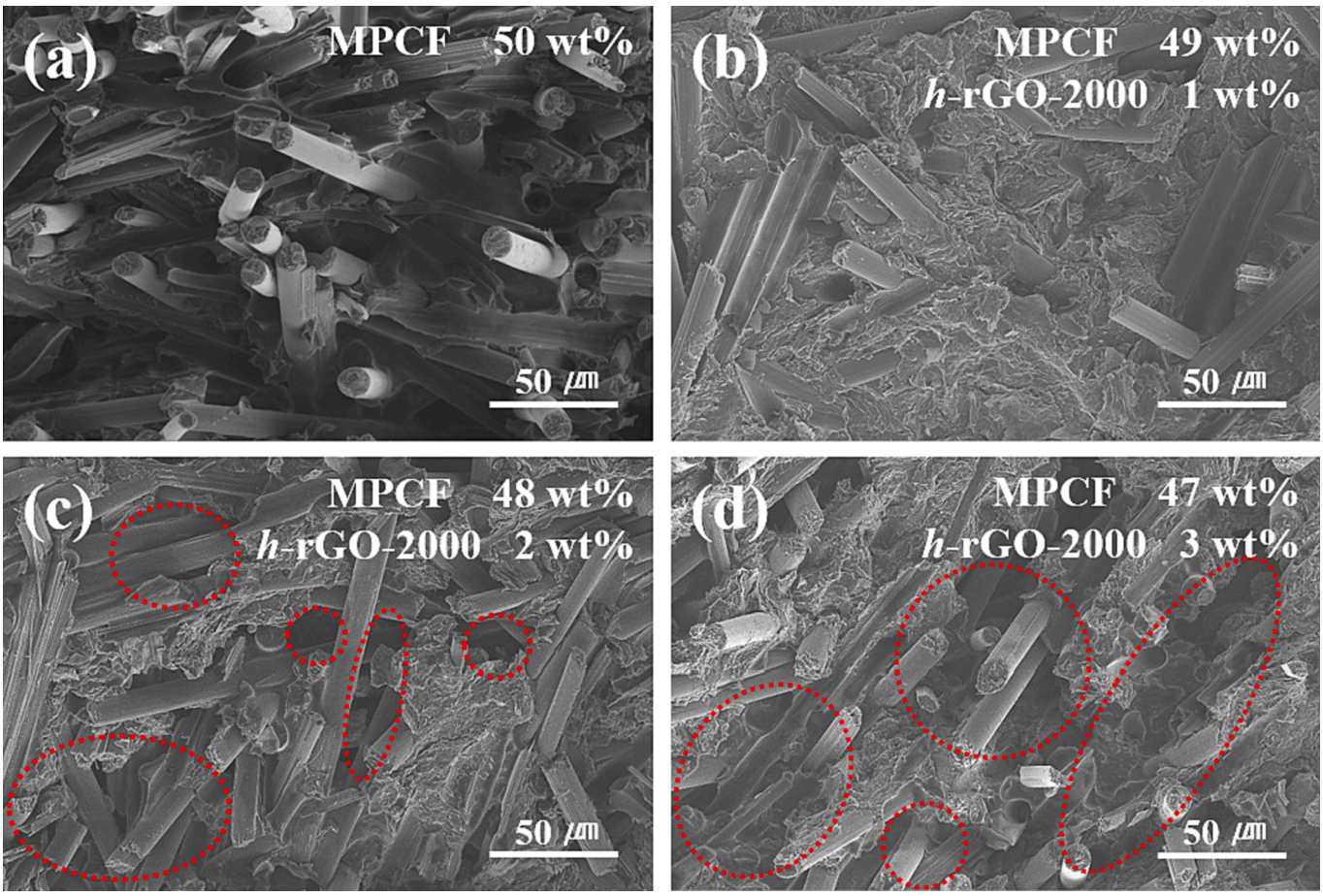

Fig. 8. FE-SEM images of epoxy-based composites with (a) 50 wt% MPCF, (b) 49 wt% MPCF and 1 wt% *h*-rGO-2000, (c) 48 wt% MPCF and 2 wt% *h*-rGO-2000, and (d) 47 wt% MPCF and 3 wt% *h*-rGO-2000.

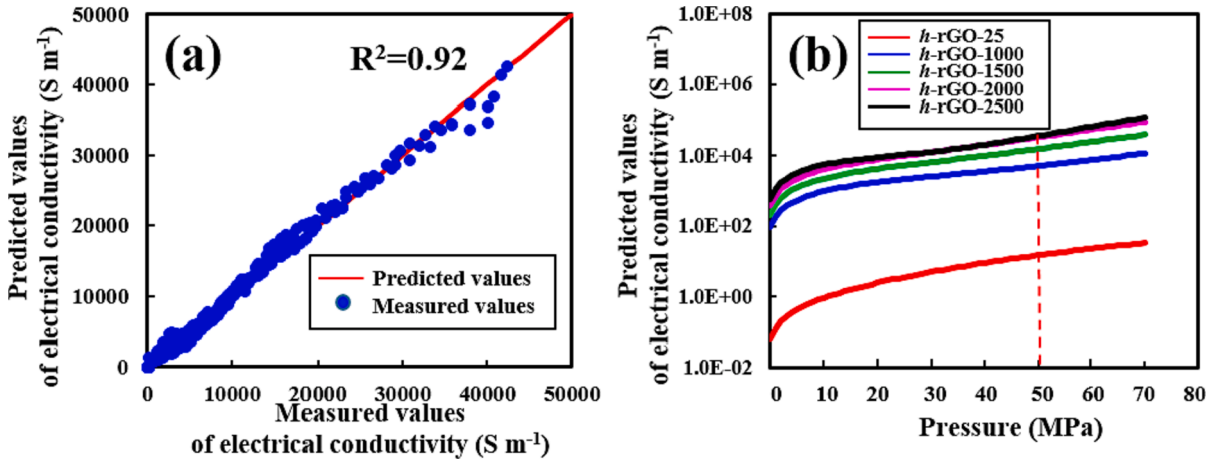

Fig. 9. (a) GPR-based predictions of electrical conductivity and (b) the parametric predictions with higher *T* and *P* values. The red dotted line indicates the pressure of 50 MPa applied in the experiments.

describe the isotropic and in-plane thermal conductivities of the epoxy composite containing rGOs and MPCFs:

$$K^*_{Iso} = 5.2\sin\left(\sqrt{\phi_c}\right)\left[\phi_g + \cos\left(\phi_g\right) + \sin\left(\phi_g\right)\right] - 3\sin[\sin(\phi_c)]\sin\left(T - \phi_g\right) + 0.13 \quad (5)$$

$$K^*_{In} = 1.5\cos\left(T - \phi_g\right) + 1.5\left(T{\cdot}\phi_g\right)^{0.25} + 0.1{\cdot}\cos\left(\phi_g\right)\sqrt{T{\cdot}\phi_g} + 5.8 \quad (6)$$

where K^*_{Iso} and K^*_{In} denote the isotropic and in-plane thermal conductivities of the composites, respectively; T is the applied temperature during the composite fabrication process, and ϕ_g and ϕ_c signify the weight fractions of the rGO and MPCF fillers, respectively.

Fig. 10a and 10b show the agreement between the measured and predicted isotropic and in-plane thermal conductivities. The coefficient of determination (R^2) for the isotropic thermal conductivity was considerably lower than that for the in-plane thermal conductivity

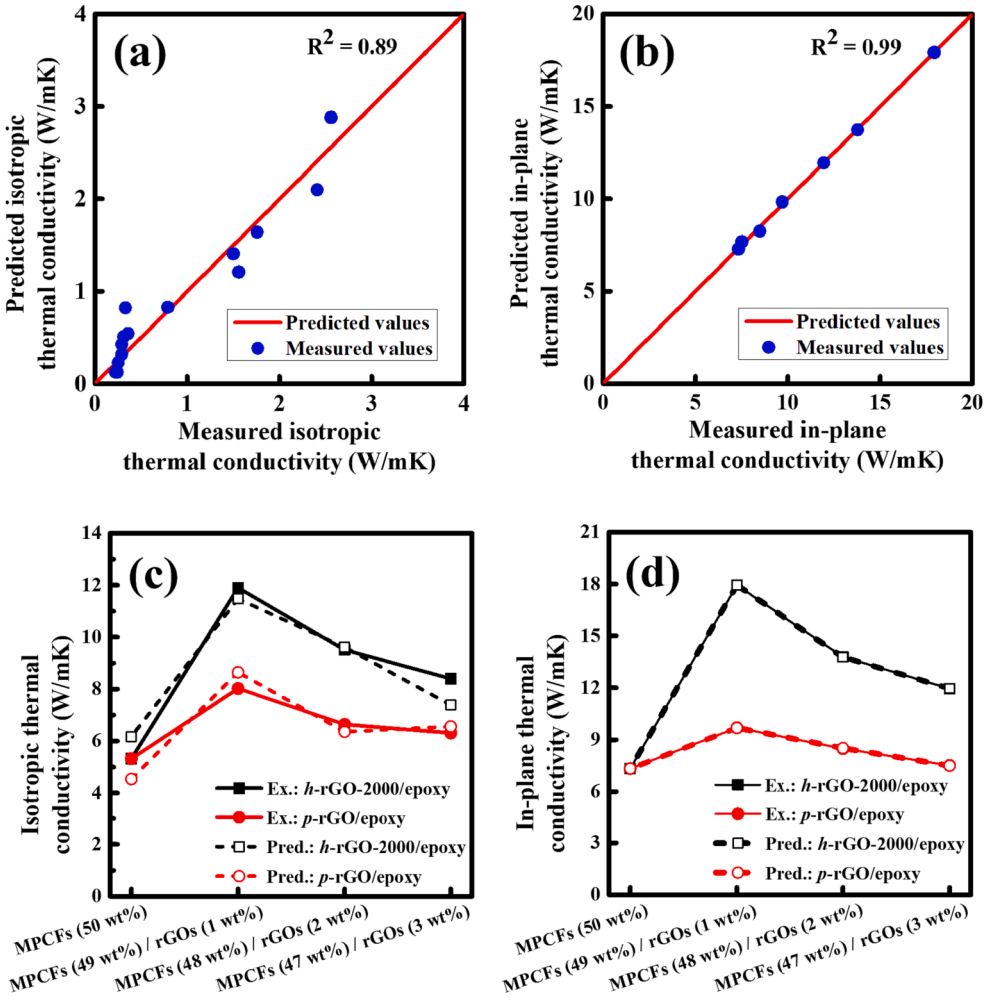

Fig. 10. GPR-based predictions of the (a) isotropic and (b) in-plane thermal conductivities of rGO/epoxy composites and comparisons of the experimental and predicted (c) isotropic and (d) in-plane thermal conductivities.

owing to the different patterns in the data. Despite the relatively small set of training data, the predicted isotropic and in-plane thermal conductivities of epoxy-based composites containing various ratios of rGOs and MPCFs are similar to the experimentally observed values in most cases (Fig. 10c and 10d).

Notably, the isotropic thermal conductivity was predicted from the data presented in Fig. 4 and Fig. 7; however, in the case of the in-plane thermal conductivity, only the data shown in Fig. 7 were applied for training. Comparing the experimental and predicted values shown in Fig. 10a and 10b, the model predicts the in-plane thermal conductivity more accurately than the isotropic thermal conductivity. Nevertheless, it is anticipated that the prediction accuracy for in-plane thermal conductivity under diverse conditions will be limited owing to the narrow range of conditions examined and the notably small quantity of training data available. For instance, the constant ϕ_c is omitted from the GPR-derived in-plane thermal conductivity equation, Eq. (6). In other words, the accuracy represented in Fig. 10b and 10d was derived without excluding the effect on the MPCFs. Hence, the accuracy of the prediction may be poor for specimens containing a large amount of MPCFs. Additional parametric analysis based on the derived model was conducted using 0–10 wt% rGO content. The results are included in Fig. S6, which indicate that using approximately 6–7 wt% rGO content and higher HT temperatures are necessary to attain higher thermal conductivity. Nevertheless, these findings are constrained to the specific experimental range evaluated in the study. Therefore, predictions for specimens beyond this range may not be precise. While the GPR model compensates for the smaller dataset by prioritizing data quality and distribution, it imposes constraints on the generalizability of the current findings. In future, we will expand the experimental dataset, thereby enhancing the robustness and accuracy of our ML models.

5. Conclusions

This study reported on investigating the structural and physical changes in rGOs induced by high-temperature thermal reduction and the effects of *h*-rGO fillers as reinforcements on the thermal conductivity of polymer composites. The *p*-rGO exhibited low crystallinity owing to the presence of defect sites and O-containing functional groups formed during the oxidation process. The number of structural defects and O-containing functionalities on the rGO surface significantly decreased with increasing HT temperature, thereby restoring the graphitic structure of the rGO. The thermal conductivities of the rGO/epoxy composites were proportional to the temperature at which the rGOs underwent HT. Moreover, the *h*-rGO fillers significantly increased the thermal conductivity of the polymer composites; notably, the composite with 10 wt% *h*-rGO-2500 exhibited an 11.6-fold increase in thermal conductivity with respect to that of the composite with 10 wt% *p*-rGO filler. Thus, the thermal conductivity of this heat-treated filler is far superior to existing commercial carbon materials. In particular, a hybrid filler consisting of MPCFs and *h*-rGO-2000 in a weight ratio of 49:1 exhibited a strong synergistic effect on the thermal conductivity enhancement in the MPCF–rGO/epoxy composites. The properties of the rGOs and

composites were also predicted from their HT temperatures and material compositions using an ML-based GPR method. The GPR method developed in this study showed excellent performance in the overall prediction of the material properties and is expected to be applied in the future for the analysis of similar materials. We anticipate that our method for producing lightweight heat dissipation materials with high thermal conductivity will contribute to the advancement of heat management technologies. This innovation has the potential to revolutionize the thermal performance of electronic devices, encompassing wearable and flexible technologies, as well as electric vehicle battery systems, light-emitting diode lighting systems, power equipment, and aerospace components. By ensuring more efficient heat dissipation, it can extend the lifespan and optimize the overall functionality of these applications. Moreover, we believe that this study can offer important information to help determine a trade-off between the reduction costs of rGO and thermal conductivities of polymer composites in industrial manufacturing, with respect to thermally conductive polymer composites containing rGOs.

CRediT authorship contribution statement

Yun Seon Lee: Conceptualization, Data curation, Investigation, Methodology, Formal analysis, Writing – original draft. **Nam Ryeol Kim:** Data curation, Investigation, Methodology, Formal analysis, Writing – original draft. **Sang Ki Park:** Data curation, Methodology, Formal analysis. **Yong-il Ko:** Data curation, Formal analysis, Methodology. **Yunjae Shin:** Data curation, Formal analysis, Methodology. **Beomjoo Yang:** Investigation, Methodology, Supervision, Writing – original draft. **Cheol-Min Yang:** Conceptualization, Funding acquisition, Investigation, Methodology, Project administration, Supervision, Validation, Writing – review & editing.

Declaration of competing interest

The authors declare that they have no known competing financial interests or personal relationships that could have appeared to influence the work reported in this paper.

Data availability

Data will be made available on request.

Acknowledgements

This research was supported by the Korea Institute of Science and Technology (KIST) Institutional Program and the Technology Innovation Program (20006820), funded by the Ministry of Trade, Industry & Energy (MOTIE) of Korea.

Appendix A. Supplementary material

Supplementary data to this article can be found online at https://doi.org/10.1016/j.apsusc.2023.159140.

References

[1] H.Y. Chen, V.V. Ginzburg, J. Yang, Y.F. Yang, W. Liu, Y. Huang, L.B. Du, B. Chen, Thermal conductivity of polymer-based composites: Fundamentals and applications, Prog. Polym. Sci. 59 (2016) 41–85.
[2] F. Gong, H. Li, W. Wang, D. Xia, Q. Liu, D.V. Papavassiliou, Z. Xu, Recent advances in graphene-based free-standing films for thermal management: synthesis, properties, and applications, Coatings 8 (2018) 63.
[3] A.L. Moore, L. Shi, Emerging challenges and materials for thermal management of electronics, Mater. Today 17 (2014) 163–174.
[4] Y. Wang, X. Zhang, X. Ding, Y. Li, P. Zhang, M. Shu, Q. Zhang, Y. Gong, K. Zheng, B. Wu, X. Tian, Enhanced thermal conductivity of carbon nitride-doped graphene/polyimide composite film via a “deciduous-like” strategy, Compos. Sci. Tech. 205 (2021), 108693.
[5] Z. Han, A. Fina, Thermal conductivity of carbon nanotubes and their polymer nanocomposites: a review, Prog. Polym. Sci. 36 (2011) 914–944.
[6] H. Song, J. Liu, B. Liu, J. Wu, H.-M. Cheng, F. Kang, Two-dimensional materials for thermal management applications, Joule 2 (2018) 442–463.
[7] C.L. Huang, X. Qian, R.G. Yang, Thermal conductivity of polymers and polymer nanocomposites, Mater. Sci. Eng. R Rep. 132 (2018) 1–22.
[8] H. Guo, B. Hu, Q. Wang, J. Liu, M. Li, B. Li, Horizontally aligned graphene/silver heterostructure for anisotropically highly thermoconductive polymer-based composites by stress-induced assembly, Appl. Surf. Sci. 615 (2023), 156404.
[9] L. Yu, J.S. Park, Y.-S. Lim, C.S. Lee, K. Shin, H.J. Moon, C.-M. Yang, Y.S. Lee, J. H. Han, Carbon hybrid fillers composed of carbon nanotubes directly grown on graphene nanoplatelets for effective thermal conductivity in epoxy composites, Nanotechnology 24 (2013), 155604.
[10] J. Wang, P. Ren, Z. Chen, T. Wu, F. Wang, C. You, Enhanced thermal conductivity of epoxy composites reinforced with oriented polydopamine-graphene foam complexed by metal ions, Appl. Surf. Sci. 610 (2023), 155309.
[11] X. Huang, C. Zhi, Y. Lin, H. Bao, G. Wu, P. Jiang, Y.-W. Mai, Thermal conductivity of graphene-based polymer nanocomposites, Mater. Sci. Eng. R Rep. 142 (2020), 100577.
[12] X. Wu, B. Tang, J. Chen, L. Shan, Y. Gao, K. Yang, Y. Wang, K. Sun, R. Fan, J. Yu, Epoxy composites with high cross-plane thermal conductivity by constructing all-carbon multidimensional carbon fiber/graphite networks, Compos. Sci. Tech. 203 (2021) 108610.
[13] Y. Sun, L. Chen, J. Lin, P. Cui, M. Li, X. Du, Thermal conductivity of epoxy composites filled by thermally reduced graphite oxide with different reduction degree, J. Compos. Mater. 51 (2017) 1743–1752.
[14] Y. Guo, K. Ruan, X. Shi, X. Yang, J. Gu, Factors affecting thermal conductivities of the polymers and polymer composites: a review, Compos. Sci. Tech. 193 (2020), 108134.
[15] K.S. Novoselov, A.K. Geim, S.V. Morozov, D. Jiang, Y. Zhang, S.V. Dubonos, I. V. Grigorieva, A.A. Firsov, Electric field effect in atomically thin carbon films, Science 306 (2004) 666–669.
[16] V.B. Mohan, K.-T. Lau, D. Hui, D. Bhattacharyya, Graphene-based materials and their composites: a review on production, applications and product limitations, Compos. Part B Eng. 142 (2018) 200–220.
[17] M. Rafiee, F. Nitzsche, J. Laliberte, S. Hind, F. Robitaille, M. Labrosse, Thermal properties of doubly reinforced fiberglass/epoxy composites with graphene nanoplatelets, graphene oxide and reduced-graphene oxide, Compos. Part B Eng. 164 (2019) 1–9.
[18] T. Jiao, B. Han, L. Zhao, Z. Zhang, Y. Zeng, D. Li, K. Zhang, Q. Deng, Y. Zhao, Z. Li, Pie-rolling-inspired construction of vertical carbon fiber high thermal conductivity hybrid networks, Appl. Surf. Sci. 618 (2023), 156711.
[19] Y. Zhao, Z. Wu, S. Guo, Z. Zhou, Z. Miao, S. Xie, R. Huang, L. Li, Hyperbranched graphene oxide structure-based epoxy nanocomposite with simultaneous enhanced mechanical properties, thermal conductivity, and superior electrical insulation, Compos. Sci. Tech. 217 (2022), 109082.
[20] A.A. Balandin, S. Ghosh, W. Bao, I. Calizo, D. Teweldebrhan, F. Miao, C.N. Lau, Superior thermal conductivity of single-layer graphene, Nano Lett. 8 (2008) 902–907.
[21] S. Stankovich, R.D. Piner, X. Chen, N. Wu, S.T. Nguyen, R.S. Ruoff, Stable aqueous dispersions of graphitic nanoplatelets via the reduction of exfoliated graphite oxide in the presence of poly (sodium 4-styrenesulfonate), J. Mater. Chem. 16 (2006) 155–158.
[22] D.V. Kosynkin, A.L. Higginbotham, A. Sinitskii, J.R. Lomeda, A. Dimiev, B.K. Price, J.M. Tour, Longitudinal unzipping of carbon nanotubes to form graphene nanoribbons, Nature 458 (2009) 872–876.
[23] Y.-Y. Zhang, Y. Cheng, Q.X. Pei, C.M. Wang, Y. Xiang, Thermal conductivity of defective graphene, Phys. Lett. A 376 (2012) 3668–3672.
[24] Z.Y. Xia, S. Pezzini, E. Treossi, G. Giambastiani, F. Corticelli, V. Morandi, A. Zanelli, V. Bellani, V. Palermo, The exfoliation of graphene in liquids by electrochemical, chemical, and sonication-assisted techniques: a nanoscale study, Adv. Funct. Mater. 23 (2013) 4684–4693.
[25] M.I. Kairi, S. Dayou, N.I. Kairi, S.A. Bakar, B. Vigolo, A.R. Mohamed, Toward high production of graphene flakes-a review on recent developments in their synthesis methods and scalability, J. Mater. Chem. A 6 (2018) 15010–15026.
[26] Z.S. Wu, W. Ren, L. Gao, J. Zhao, Z. Chen, B. Liu, D. Tang, B. Yu, C. Jiang, H.-M. Cheng, Synthesis of graphene sheets with high electrical conductivity and good thermal stability by hydrogen arc discharge exfoliation, ACS Nano 3 (2009) 411–417.
[27] Y. Zhang, L. Zhang, C. Zhou, Review of chemical vapor deposition of graphene and related applications, Acc. Chem. Res. 46 (2013) 2329–2339.
[28] Q.M. Gong, Z. Li, Y. Wang, B. Wu, Z. Zhang, J. Liang, The effect of high-temperature annealing on the structure and electrical properties of well-aligned carbon nanotubes, Mater. Res. Bull. 42 (2007) 474–481.
[29] S. Mikhailov, Physics and applications of graphene: experiments, BoD Books on Demand, 2011.
[30] C. Zeng, S. Lu, L. Song, X. Xiao, J. Gao, L. Pan, Z. He, J. Yu, Enhanced thermal properties in a hybrid graphene–alumina filler for epoxy composites, RSC Adv. 5 (2015) 35773–35782.
[31] M.W. Akhtar, Y.S. Lee, D.J. Yoo, J.S. Kim, Alumina-graphene hybrid filled epoxy composite: quantitative validation and enhanced thermal conductivity, Compos. Part B Eng. 131 (2017) 184–195.
[32] S.Y. Kim, H.G. Jang, C.-M. Yang, B.J. Yang, Multiscale prediction of thermal conductivity for nanocomposites containing crumpled carbon nanofillers with interfacial characteristics, Compos. Sci. Tech. 155 (2018) 169–176.

[33] D. He, Z. Peng, W. Gong, Y. Luo, P. Zhao, L. Kong, Mechanism of a green graphene oxide reduction with reusable potassium carbonate, RSC Adv. 5 (2015) 11966–11972.
[34] A. Ganguly, S. Sharma, P. Papakonstantinou, J. Hamilton, Probing the thermal deoxygenation of graphene oxide using high-resolution in situ X-ray-based spectroscopies, J. Phys. Chem. C 115 (2011) 17009–17019.
[35] F.C. Tai, C. Wei, S.H. Chang, W.S. Chen, Raman and X-ray diffraction analysis on unburned carbon powder refined from fly ash, J. Raman Spectrosc. 41 (2010) 933–937.
[36] K.N. Kudin, B. Ozbas, H.C. Schniepp, R.K. Prud'Homme, I.A. Aksay, R. Car, Raman spectra of graphite oxide and functionalized graphene sheets, Nano Lett. 8 (2008) 36–41.
[37] M.R. D'Oliveira, J. Rabelo, A.G. Veiga, C.A. Chagas, M. Schmal, In situ DRIFTS investigation of ethylene oxidation on Ag and Ag/Cu on reduced graphene oxide, Catal. Lett. 150 (2020) 1–13.
[38] C.Y. Su, Y. Xu, W. Zhang, J. Zhao, A. Liu, X. Tang, C.-H. Tsai, Y. Huang, L.J. Li, Highly efficient restoration of graphitic structure in graphene oxide using alcohol vapors, ACS Nano 4 (2010) 5285–5292.
[39] S. Sahoo, G. Khurana, S.K. Barik, S. Dussan, D. Barrionuevo, R.S. Katiyar, In situ Raman studies of electrically reduced graphene oxide and its field-emission properties, J. Phys. Chem. C 117 (2013) 5485–5491.
[40] B. Rajagopalan, J.S. Chung, Reduced chemically modified graphene oxide for supercapacitor electrode, Nanoscale Res. Lett. 9 (2014) 1–10.
[41] F. Ricciardella, E. Massera, T. Polichetti, M.L. Miglietta, G.D. Francia, A calibrated graphene-based chemi-sensor for sub parts-per-million NO_2 detection operating at room temperature, Appl. Phys. Lett. 104 (2014), 183502.
[42] F.T. Johra, J.-W. Lee, W.-G. Jung, Facile and safe graphene preparation on solution based platform, J. Ind. Eng. Chem. 20 (2014) 2883–2887.
[43] W. Gao, L.B. Alemany, L. Ci, P.M. Ajayan, New insights into the structure and reduction of graphite oxide, Nat. Chem. 1 (2009) 403–408.
[44] Y. Huang, Q. Gong, Q. Zhang, Y. Shao, J. Wang, Y. Jiang, M. Zhao, D. Zhuang, J. Liang, Fabrication and molecular dynamics analyses of highly thermal conductive reduced graphene oxide films at ultra-high temperatures, Nanoscale 9 (2017) 2340–2347.
[45] J. Che, K. Wu, Y. Lin, K. Wang, Q. Fu, Largely improved thermal conductivity of HDPE/expanded graphite/carbon nanotubes ternary composites via filler network-network synergy, Compos. Appl. Sci. Manuf. 99 (2017) 32–40.
[46] Y.-J. Xiao, W.-Y. Wang, X.-J. Chen, T. Lin, Y.-T. Zhang, J.-H. Yang, Y. Wang, Z.-W. Zhou, Hybrid network structure and thermal conductive properties in poly (vinylidene fluoride) composites based on carbon nanotubes and graphene nanoplatelets, Compos. Appl. Sci. Manuf. 90 (2016) 614–625.
[47] Z. Barani, A. Mohammadzadeh, A. Geremew, C.-Y. Huang, D. Coleman, L. Mangolini, F. Kargar, A.A. Balandin, Thermal properties of the binary-filler hybrid composites with graphene and copper nanoparticles, Adv. Funct. Mater. 30 (2020) 1904008.
[48] G.-Q. Qi, J. Yang, R.-Y. Bao, Z.-Y. Liu, W. Yang, B.-H. Xie, M.-B. Yang, Enhanced comprehensive performance of polyethylene glycol based phase change material with hybrid graphene nanomaterials for thermal energy storage, Carbon 88 (2015) 196–205.
[49] Y. Liu, K. Wu, M. Lu, J. Shi, L. Liang, M. Lu, Enhanced thermal conductivity of bio-based epoxy-graphite nanocomposites with degradability by facile in-situ construction of microcapsules, Compos. B Eng. 218 (2021), 108936.
[50] K.T.S. Kong, M. Mariatti, A.A. Rashid, J.J.C. Busfield, Enhanced conductivity behavior of polydimethylsiloxane (PDMS) hybrid composites containing exfoliated graphite nanoplatelets and carbon nanotubes, Compos. B Eng. 58 (2014) 457–462.
[51] S.Y. Kim, Y.J. Noh, J. Yu, Thermal conductivity of graphene nanoplatelets filled composites fabricated by solvent-free processing for the excellent filler dispersion and a theoretical approach for the composites containing the geometrized fillers, Compos. Appl. Sci. Manuf. 69 (2015) 219–225.
[52] W.-B. Zhang, Z.-X. Zhang, J.-H. Yang, T. Huang, N. Zhang, X.T. Zheng, Y. Wang, Z.-W. Zhou, Largely enhanced thermal conductivity of poly (vinylidene fluoride)/carbon nanotube composites achieved by adding graphene oxide, Carbon 90 (2015) 242–254.
[53] C.B. Kim, J. Lee, J. Cho, M. Goh, Thermal conductivity enhancement of reduced graphene oxide via chemical defect healing for efficient heat dissipation, Carbon 139 (2018) 386–392.
[54] W. Jang, S. Lee, N.R. Kim, H. Koo, J. Yu, C.-M. Yang, Eco-friendly and scalable strategy to design electrically insulating boron nitride/polymer composites with high through-plane thermal conductivity, Compos. B Eng. 248 (2023), 110355.
[55] B.U. Durmaz, M.G. Atılgan, A. Aytac, A comparative study of graphene oxide or chemically reduced graphene oxide filled poly (ethylene terephthalate)/poly (butylene terephthalate)/graphene nanocomposites, Iran Polym. J. 31 (2022) 991–1002.
[56] G. Trusiano, S. Matta, M. Bianchi, L.G. Rizzi, A. Frache, Evaluation of nanocomposites containing graphene nanoplatelets: mechanical properties and combustion behavior, Polym. Eng. Sci. 59 (2019) 2062–2071.
[57] A. Graziano, O.A.T. Dias, C. Garcia, S. Jaffer, J. Tjong, M. Sain, Impact of reduced graphene oxide on structure and properties of polyethylene rich binary systems for performance-based applications, Polymer 202 (2020), 122622.
[58] R. Aradhana, S. Mohanty, S.K. Nayak, Comparison of mechanical, electrical and thermal properties in graphene oxide and reduced graphene oxide filled epoxy nanocomposite adhesives, Polymer 141 (2018) 109–123.
[59] Y.S. Lee, J. Yu, S.E. Shim, C.-M. Yang, Synergistic effects of hybrid carbonaceous fillers of carbon fibers and reduced graphene oxides on enhanced heat-dissipation capability of polymer composites, Polymers 12 (2020) 909.
[60] Y.S. Lee, S.-Y. Lee, K.S. Kim, S. Noda, S.E. Shim, C.-M. Yang, Effective heat transfer pathways of thermally conductive networks formed by one-dimensional carbon materials with different sizes, Polymers 11 (2019) 1661.